2B.3 INITIALIZATION AND FORECASTING OF THUNDERSTORMS: A CASE STUDY USING STEPS DATA

Juanzhen Sun*
Jay Miller

National Center for Atmospheric Research, Boulder, Colorado

1. INTRODUCTION

Numerical prediction of thunderstorms drew a good deal of attention in the last decade. A number of studies have focused on developing techniques that can be used to initialize a cloud-scale numerical model with high-resolution Doppler radar data and examining the predictability of thunderstorms starting from more realistic initial conditions (i.e, Weygadt et al. 2001, Montmerle et al. 2001). In this study, we conduct initilization and forecasting experiments of the supercell storm of June 29 2000 observed during STEPS (Severe Thunderstorm Electrification and Precipitation Study). Our main objective is to study the predictability of the storm when initialized with radar data using an advanced data assimilation technique.

2. CASE DESCRIPTION

The June 29 2000 supercell storm occurred near Bird City, Kansas. This supercell storm was observed by the WSR-88D radar located at Goodland, Kansas and two research radars (CHILL and SPOL). It was formed along an advancing surface boundary propagating to the southeast. The first echo appeared on radar around 2130 UTC. The pre-storm environmental sounding observed at 2022 UTC from the NCAR Mobil GPS/Loran Sounding System (MGLASS) is interpolated to the model levels and shown in Fig. 1. The sounding indicates that a southerly component to the low-level flow and veering winds up to the tropopause and the environment is abundant in CAPE (Convective Available Potential Energy). The storm's track is illustrated by the 40 dBZ contour line plotted every 20 min. in Fig. 2. The position of the three radars is also indicated in Fig. 2 . The storm propagated southeastward, from about 295^o at a speed of about 9.7 ms^{-1}, before ~2325 UTC. It then turned right from 295^o to 330^o and moved with a velocity of 8.9 ms^{-1} . A F1 tornado was reported at 2328 UTC. Reflectivities of near 65 dBZ, that are believed to represent hail, began to exhibit at 2230 UTC.

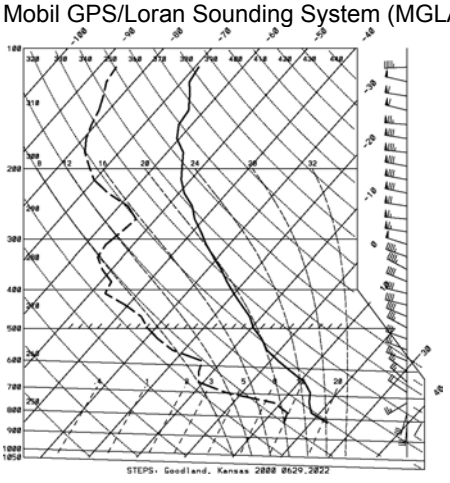

Fig. 1 Observed sounding at 2022 UTC.

* *Corresponding author address*: Juanzhen Sun, NCAR, Boulder, Co 80307; sunj@ucar.edu

3. METHOD OF INITIALIZATION

The supercell storm described above was initialized at 2235 UTC using the observations from the WSR-88D radar KGLD located at Goodland, Kansas. NCAR's four-dimensional variational (4D-Var) data assimilation system VDRAS (Variational Doppler Radar Analysis System) was used for the initialization experiments (Sun and Crook 1997). Two-hour numerical forecast was performed after the initialization using the cloud model in VDRAS. The numerical domain covers an area of 140kmx140km and extends to the height of 15

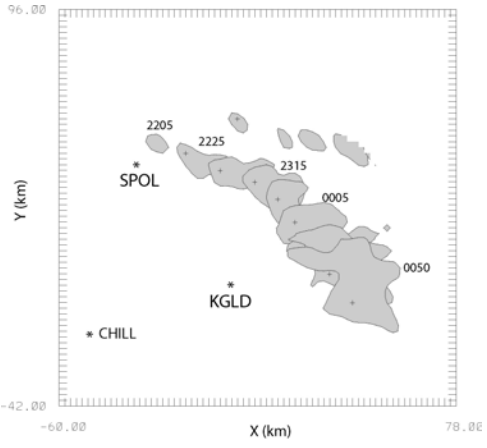

Fig. 2 40 dBZ contours indicating the storm location at z=0.75 km with a 20 min interval. The "+" sign marks the maximum reflectivity.

km. The resolution is 2 km in the horizontal and 500 m in the vertical. The temporal resolution is 5 seconds. A cycling procedure is implemented in VDRAS. The entire assimilation period of 30 minutes includes two assimilation cycles and one forecast cycle (10 min each). Each assimilation cycle assimilates two volumes of data. These data are interpolated to Cartesian grid of the same resolution as the numerical model. At every other time step, a portion of data, whose observation time is within 10 seconds of that time step, is assimilated. The data assimilation can be performed only using one assimilation cycle starting at 222500 UTC or the assimilation-forecast-assimilation procedure that spans a period of 30 minutes. We have found that the cycling procedure improves the accuracy of the initial conditions and hence the prediction.

In each assimilation cycle, a trajectory, that optimally fit the observations distributed in the assimilation window of 10 minutes, is sought by minimizing the following cost function:

$$J = (x_0 - x_b)^T B^{-1}(x_0 - x_b) + \sum_{\sigma,t} [\eta_v (v_r - v_r^o)^2 + \eta_q (q_r - q_r^o)^2] + J_p \quad (2.1)$$

where x_0 represents the model state at the beginning of the assimilation window and x_b the previous forecast for the second assimilation cycle or a large-scale background for the first assimilation cycle. The symbol B denotes the background covariance matrix and is assumed diagonal and constant in this study. The variable v_r is the radial velocity computed from the model velocity components; v_r^o is the observed radial velocity; q_r is the rain water mixing ratio from the model; and q_r^o is the estimated rain water mixing ratio from the reflectivity observation using a Z-q_r Conversion formula. The quantities η_v and η_q are weighting coefficients for radial velocity and reflectivity, respectively. The summation is over space and time. The symbol J_p denotes the spatial and temporal smoothness penalty term. The function of the smoothness penalty term is to ensure a smooth fit to the observations. Since the reduction of the cost function slows down significantly after 70 iterations, the minimization is terminated after 70 iterations.

4. EXPERIMENTS AND RESULTS

Experiments with the observed sounding at 2022 UTC (Fig. 1) failed to initiate convection. After carefully examining this sounding against mesonet observations and a VAD (Velocity Azimuth Display) analysis obtained using the KGLD radar radial velocity observations at 2130 UTC, we found there were significant differences. The low-level temperature and dew-point temperature were then adjusted to match the surface observations and to keep the air well mixed in the boundary layer. In addition, smoothing is applied to the dew-point profile. The wind profile is replaced by the VAD analysis in the low-level (below 1.75 km) and the average wind between the observations at 2022 UTC and 2338 UTC above 4.75 km. A cubic spline interpolation was used to determine the wind between 1.75 km and 4.75 km. The main difference is in the mid-level where the northwest wind is increased after the modification. The shear in the north-south direction is reduced according to the VAD analysis.

After the 30-min data assimilation period, a complete set of initial conditions is obtained at 223500 UTC. Fig. 3 shows some of the analysis fields in a vertical cross section through the center of the storm at 2235 UTC. The magnitude of the updraft (Fig. 3a) is about 15 m s-1. There is a positive temperature perturbation of over 2 ^oC in the mid-level and a weak cold pool near the surface (Fig. 3b). The maximum cloud water mixing ratio is a little bit over 2 g kg^{-1}. The

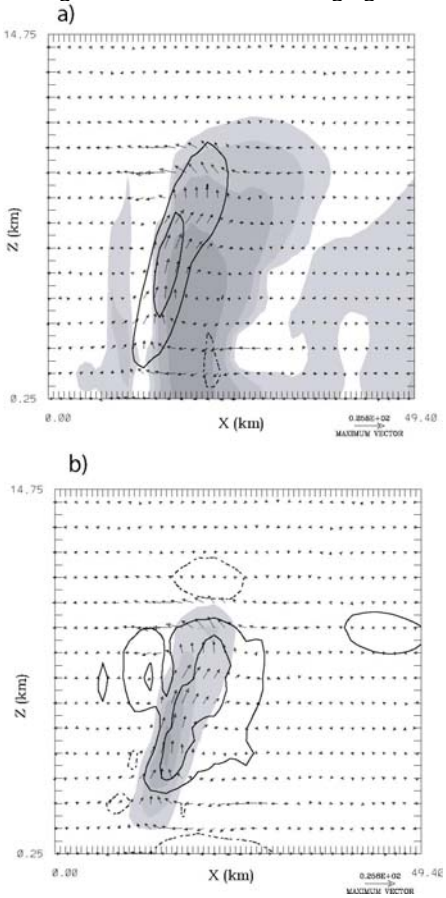

Fig. 3 Vertical cross-section of the analysis at 2235 UTC. a) Reflectivity (shade with 20 dBZ increment starting from 20 dBZ) and vertical velocity (-2.5,5,and 10 m/s contours are shown); b) Cloud water mixing ratio (shade with 0.5 g/kg increment starting from 0.5 g/kg) and perturbation temperature (-1,1, and 2^{o}c contours are shown).

reflectivity field shown in Fig. 3a by the shaded area is converted from the analysis rain water mixing ratio.

The accuracy of the retrieved wind is verified by computing the RMS error of the radial velocity. Fig. 4 shows the vertical distribution of

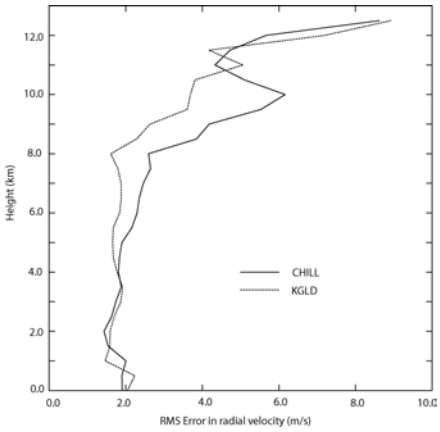

Fig. 4 Vertical profile of the RMS radial velocity error of the analysis at 2235 UTC.

the RMS error computed using radial velocity data from the KGLD radar and from the CHILL radar. Since the KGLD data are used in VDRAS as observations, the RMS error with respect to the KGLD data represents the final fit to the observation. It is seen from Fig. 4, the RMS errors are generally smaller than 2 m/s below the level of 6 km. The errors increase rapidly above 8 km. It is speculated that the following two factors may have caused the larger error in the upper levels: 1) the scarcity of observations; 2) the lack of ice physics in the numerical model.

Two-hour model prediction is conducted staring from the initial conditions obtained from the radar data assimilation. The performance of the forecasts is verified by computing the three-dimensional relative correlation coefficient between the forecast rainwater mixing ratio and the rainwater mixing ratio estimated from the reflectivity observation. Fig. 5 shows the rainwater correlation coefficient of the two-hour prediction for two experiments: one with the assimilation-forecast-assimilation cycle (solid line) and the other with an assimilation cycle only (dashed line). Both prediction starts at 223500 UTC. It is evident that the correlation is improved especially in the second hour when the cycling procedure is implemented.

Fig. 6 compares the track of the simulated storm with the observation by plotting the 40 dBZ contours at z=0.75 km with a 20 min interval. The "+" sign indicates the location of the maximum reflectivity. The predicted storm track from the experiment (Fig. 6b) shows a good agreement with the observation (Fig. 6a). It made the right turn at about the same time as in the observation. Fig. 6a also shows a weaker storm located northeast of the supercell storm. This storm was propagated by the mean wind and did not

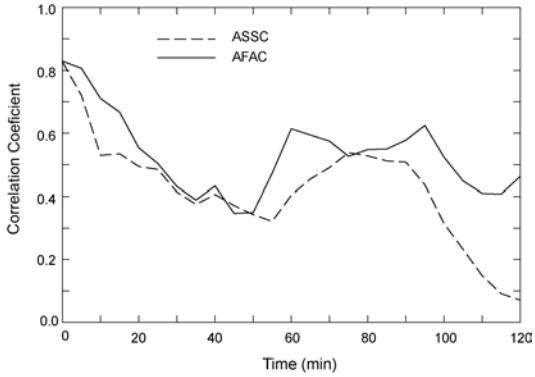

Fig. 5 Rain water correlation coefficient with respect to forecast time.

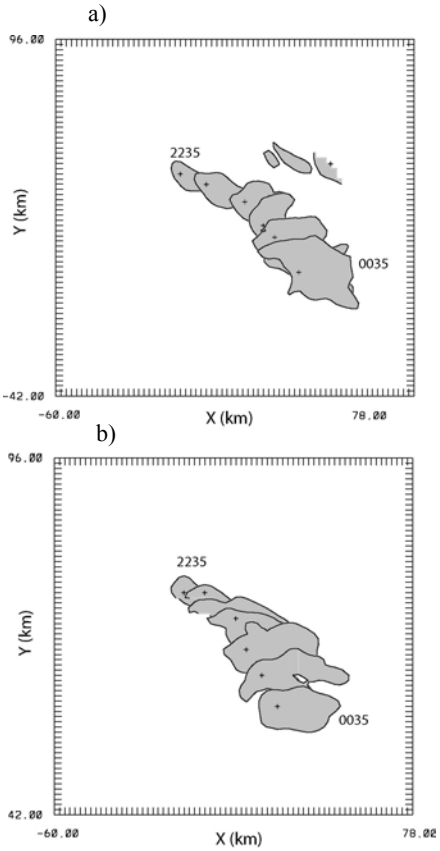

Fig. 6 Storm position indicated by the 40 dBZ contour lines at z=0.75 km with a 20 min interval for a) observation and b) forecast. The "+" sign marks the location of the maximum reflectivity.

become a supercell. The analysis captures this storm but is weaker than the observation. It is not shown in Fig. 6b because the storm is not strong enough to have a 40 dBZ contour line.

The simulated storm at 233500 (1-hour forecast) is compared with the triple-Doppler synthesis. Fig. 7 shows the reflectivity (shaded) , the vertical velocity (contour) and the velocity vector at m=1.75 km from the synthesis (Fig. 7a) and from the numerical forecast (Fig. 7b). Note that the domain in Fig. 7 is reduced from the full

simulation domain. Both the synthesis and the forecast shows an updraft located southwest of the storm. The updraft in the forecast is stronger than in the synthesis at this level. The forecast reflectivity is less concentrated in the west as in the observation. There is a stronger northerly flow entering into the storm in the forecast.

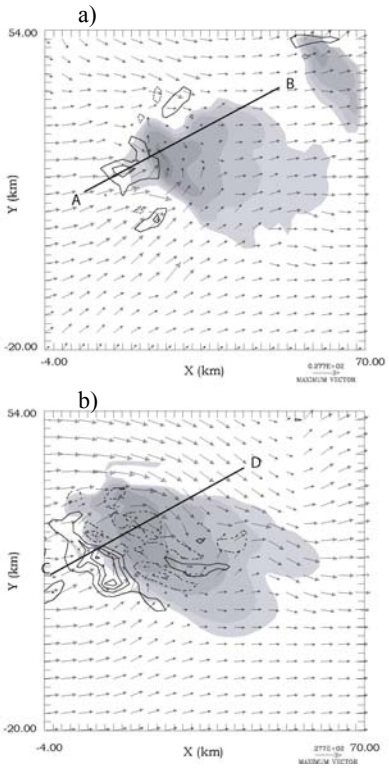

Fig. 7 Reflectivity (shade with 20 dBZ increment starting from 20 dBZ), vertical velocity (contour with an interval of 2.5 m/s and the zero contour is not shown), and velocity vector at z=1.75 km from a) triple-Doppler synthesis and b) 1-hour forecast.

Fig. 8 compares the same fields as in Fig.7 but in a vertical cross section through the line AB in Fig. 7a and CD in Fig. 7b. Both the synthesis and the forecast show two updraft centers. The maximum values of the updraft in both cross-sections are over 30 m/s. The biggest difference in the two vertical velocity fields is the absence of the downdraft on the upwind flank in the predicted storm.

5. CONCLUSIONS

From this case study, we draw the following conclusions:

1.The data assimilation using the 4D-Var technique and high-resolution radar data is able to provide initial conditions for all of the prognostic variables of a cloud-scale numerical model simultaneously.

2.The two-hour prediction of the supercell storm of June 29, 2000 starting from the 4D-Var

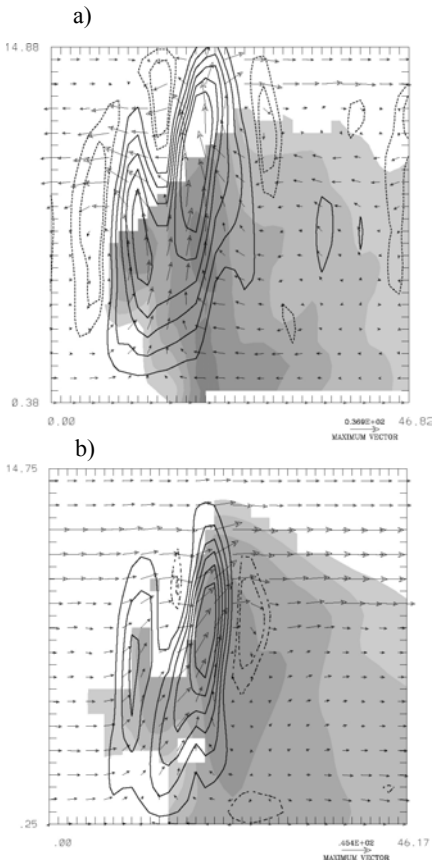

Fig. 8 Same fields as in Fig. 7 but in the vertical cross-sections indicated in Fig. 7. The contour interval is 5 m/s.

analysis using VDRAS showed good agreement with the observations

3.Comparison with the triple-Doppler synthesis shows good agreement between the synthesis and the forecast.

6. REFERENCES

Montmerle, T., A. Caya, and I. Zawadzki, 2001: Simulation of a midlatitude convective storm initialized with bistatic Doppler radar data. *Mon. Wea. Rev.*, **129**, 1949-1967.

Sun, J., and N. A. Crook, 1997: Dynamical and microphysical retrieval from Doppler radar observations using a cloud model and its adjoint: Part I. model development and simulated data experiments. J. Atmos. Sci., ***54**, 1642-1661.*

Weygandt, S., A. Shapiro, and K. Droegemier, 2002b: Retrieval of model initial fields from Single-Doppler Observations of a supercell thunderstorm. Part II: Thermodynamic retrieval and numerical prediction. Mon. Wea. Rev., 130, 454-476.